Evolution of highly eccentric binary neutron stars including tidal effects

Huan Yang,[1,2] William E. East,[2] Vasileios Paschalidis,[3] Frans Pretorius,[4,5] and Raissa F. P. Mendes[6]
[1]University of Guelph, Guelph, Ontario N2L3G1, Canada
[2]Perimeter Institute for Theoretical Physics, Waterloo, Ontario N2L2Y5, Canada
[3]Theoretical Astrophysics Program, Departments of Astronomy and Physics, University of Arizona, Tucson, Arizona 85721, USA
[4]Department of Physics, Princeton University, Princeton, New Jersey 08544, USA
[5]CIFAR, Cosmology & Gravity Program, Toronto, Ontario M5G 1Z8, Canada
[6]Instituto de Física, Universidade Federal Fluminense, Niterói, 24210-346 Rio de Janeiro, Brazil

(Received 16 June 2018; published 2 August 2018)

This work is the first in a series of studies aimed at understanding the dynamics of highly eccentric binary neutron stars, and constructing an appropriate gravitational-waveform model for detection. Such binaries are possible sources for ground-based gravitational wave detectors, and are expected to form through dynamical scattering and multibody interactions in globular clusters and galactic nuclei. In contrast to black holes, oscillations of neutron stars are generically excited by tidal effects after close pericenter passage. Depending on the equation of state, this can enhance the loss of orbital energy by up to tens of percent over that radiated away by gravitational waves during an orbit. Under the same interaction mechanism, part of the orbital angular momentum is also transferred to the star. We calculate the impact of the neutron star oscillations on the orbital evolution of such systems, and compare these results to full numerical simulations. Utilizing a post-Newtonian flux description we propose a preliminary model to predict the timing of different pericenter passages. A refined version of this model (taking into account post-Newtonian corrections to the tidal coupling and the oscillations of the stars) may serve as a waveform model for such highly eccentric systems.

DOI: 10.1103/PhysRevD.98.044007

I. INTRODUCTION

The Laser Interferometric Gravitational Wave Observatory (LIGO) and Virgo collaborations have already detected five binary black hole (BH) coalescence events [1–5] and one binary neutron star (NS) event [6]. Current event rates indicate that as LIGO and Virgo reach design sensitivity in the next few years, many more binary NS coalescences will be observed [6]. The formation of binary compact object (CO) systems can be broadly classified into two main categories: field binaries and dynamically assembled (cluster) binaries. In the first channel, the progenitor is a stellar binary where both stars eventually form COs following stellar collapse (with or without supernovae). Such a binary may gain a sizable amount of eccentricity through a supernovae kick; however subsequent gravitational wave (GW) emission will reduce the eccentricity with time, leading to a nearly circular orbit by the time the emission enters the LIGO band. In the second channel, CO binaries form through various N-body interactions that take place in dense stellar environments, including dynamical capture [7–11], and exchange interactions during binary-single and binary-binary interactions [12–14].

An exciting aspect of dynamically assembled binaries is that some fraction of these systems will emit GWs in the LIGO/Virgo bands while their orbits are highly eccentric (for order-of-magnitude estimates of these fractions see e.g., Refs. [12,14,15]). A further mechanism that can produce eccentric mergers within ground-based GW detector bands are hierarchical triple systems where a Kozai-Lidov-type resonance occurs [16–20]; such systems could form both in field and cluster environments, though for our purposes of studying eccentric mergers we will group them in the "dynamically assembled" category. Currently, the rate estimates for dynamically assembled binaries are quite uncertain, but it is possible that they contribute a non-negligible fraction of events detectable by LIGO and future ground-based GW detectors.

If a highly eccentric binary system contains one or more neutron stars it will also have distinct phenomenology. For example, the star will be tidally perturbed after each pericenter passage [21], leaving a weak, oscillatory GW imprint as a tail of the main GW burst produced at pericenter [22–24], along with possible electromagnetic emission due to crust cracking (if the pericenter distance is sufficiently small) [24,25]. Probing these post-burst NS oscillations in GWs offers an opportunity to study the oscillation modes of cold, perturbed neutron stars (NS asteroseismology), which are distinct from the modes

of a post-merger hypermassive NS remnant (see e.g., Refs. [26,27] for recent reviews on this topic).[1] Therefore it is interesting to study the dynamics of such binaries and develop an appropriate GW detection template that includes both the burst and post-burst phenomenology. However, we point out that as these post-burst oscillations are generally much weaker than the pericenter bursts, direct observation of the accompanying GWs may require at least third-generation ground-based detectors and appropriate data analysis methods, such as coherent mode stacking [31–33] (see also Refs. [34,35]).

In this work we explicitly compute the amount of energy/angular momentum deposited into the star(s) due to dynamical tidal excitations. We find that during a close passage, the change of orbital energy due to the tidal interaction may be up to tens of percent of the energy carried away by GWs during the same time, depending on the equation of state (EOS) of the star. This observation is consistent with a recent study on f-mode excitation in BH-NS binaries [36], but different from the conclusion drawn in Ref. [37], which, as we will discuss in Sec. II, we attribute to the incomplete summation of modes used in Ref. [37]. We also find that a non-negligible amount of orbital angular momentum is transferred to the star, mainly through f-mode excitations. These f-modes decay with time due to GW emission, with a quality factor that is generally very high, so that a significant fraction of the mode energy can remain by the next pericenter passage. Therefore an accurate model for the orbital evolution must include the evolution of the star's f-modes.

To model the orbit, we adopt the osculating-orbit approximation used in Ref. [38] for describing the orbital evolution of highly eccentric binary black holes (see e.g., Ref. [39] for a model of lower-eccentricity binaries). Within such an approximation, each orbital cycle is described by an eccentric orbit with fixed energy, angular momentum, and eccentricity in the post-Newtonian (PN) expansion, but these quantities change from one cycle to the next according to the accumulated flux calculated within a cycle. By definition, such an approximation fails if the conserved quantities change significantly within an orbital cycle. For the GW flux generated by the tidal excitations, we only consider Newtonian-order terms of the star(s)'s oscillations under the tidal field of the companion. Including higher-PN tidal effects may require dealing with nontrivial gauge issues connecting single star calculations to a consistent binary NS calculation [40]. For the flux generated by the orbital motion, we have used the 3PN flux formulas in Refs. [38,41].

This paper is organized as follows. In Sec. II we calculate the excitation of NS modes due to tidal interactions, and their influence on the orbital evolution by changing the orbital energy and angular momentum. In Sec. III we apply these results to polytropic stars, and compare the predictions with a full numerical calculation in Sec. IV. We review the PN description of eccentric orbits, and propose a model to describe the timing of sequential bursts of eccentric binary NS systems in Sec. V. Unless otherwise noted, we use geometric units with $G = c = 1$ throughout.

[1]Some have proposed that quasiperiodic oscillations of magnetars are associated with their crustal modes [28–30], which could be another way to realize NS asteroseismology.

II. FORMALISM

A. Mode excitation, energy and angular momentum transfer

Let us consider f-mode excitation of a NS due to the tidal field generated by its companion star. Other eigenmodes (such as p-modes) of the star are also excited by the tidal field, but their contribution to the total modal energy is much smaller than the f-modes [42], so in this work we focus only on f-modes. The generalization of the calculation performed here to additional modes is straightforward. In addition, we shall only perform the analysis of the stellar deformation to the leading, Newtonian order, because the tidal-induced energy and angular momentum transfer are already of higher PN order compared to the GW radiation backreaction. We shall also only keep the leading-order, quadrupole piece of the tidal field, as contributions from higher multipoles are negligible [42].

According to Ref. [42], the time domain equation of motion can be written as

$$\mathcal{L}\boldsymbol{\xi} = \nabla U, \tag{1}$$

where ξ is the Lagrangian displacement vector field, U is the tidal potential and $\mathcal{L}$ is a self-adjoint operator whose detailed form is not important here. Let us denote the eigenfrequency of each mode as ω_n and the eigenfunction as $\boldsymbol{\xi}^{(n)}$, where n labels the spherical harmonic indices (l, m) We define an inner product as

$$\langle \chi | \eta \rangle = \int d^3x \rho \chi^* \eta, \tag{2}$$

where ρ is the rest-mass density. The mode eigenfunctions are normalized such that $\langle \boldsymbol{\xi}^{(n)} | \boldsymbol{\xi}^{(n')} \rangle = \delta_{nn'}$. The Lagrangian displacement field can be decomposed as

$$\xi_i = \sum_{n=(l,m)} [A_n(t) \xi_i^{(n)} + \text{H.c.}], \qquad i = x, y, z, \tag{3}$$

where H.c. stands for Hermitian conjugate. As the pericenter passage time scale is much shorter than the mode decay time scale (due to GW radiation and viscous damping), and restricting to nonrotating stars as in Refs. [37,42], $\mathcal{L}$ should act solely as a second derivative when applied to functions of time. We plug Eq. (3) into

Eq. (1) and take the inner product with $\xi^{(n)}$ to obtain the time domain mode evolution equation as

$$\ddot{A}^{(n)} + \omega_n^2 A^{(n)} = \langle \boldsymbol{\xi}^{(n)} | \nabla U \rangle. \tag{4}$$

We focus on the f-modes of NSs, which can be intuitively understood as the fundamental oscillation modes of the star, and ignore the less relevant p or g overtone modes. The eigenfunction $\boldsymbol{\xi}^{(n)}$ can be expressed in vector spherical harmonics:

$$\boldsymbol{\xi}^{(n)} = (\xi_R^{(n)}(r)\mathbf{e}_r + \xi_S^{(n)}(r) r \nabla) Y_{lm}(\theta, \phi), \tag{5}$$

where the determination of $\xi_R^{(n)}$ and $\xi_S^{(n)}$ is discussed in the Appendix. Note that by writing down the mode decomposition in the time domain in Eq. (3), we need to take into account the double-counting problem, as each bracket in the summation includes both $\pm m$ modes (with m running from $-l$ to l). One way to resolve this problem is to only include modes with $m \geq 0$ in the summation, and in particular remove the Hermitian-conjugate terms for $m = 0$ modes. Another way is to allow a complex displacement field for each mode, and remove all Hermitian-conjugate terms in the summation. The reality condition for $\boldsymbol{\xi}$ will be enforced by the fact that $A^{l,m} = A^{l,-m*}$. These two methods give the same result, and we shall adopt the second approach because it is more convenient for both the time-domain and the frequency-domain analyses.

The quadrupole piece of the tidal potential can be expressed as

$$U = \frac{\mathcal{E}_{ij} x^i x^j}{2}, \tag{6}$$

with $\mathcal{E}_{ij}$ being the electric part of the tidal tensor [43,44]. During a pericenter passage, the energy deposited into the star is given by [42] [in the Lagrange description, $x_j \to x_j + \xi_j$, and we neglect $\mathcal{O}(\xi^2)$ terms]

$$\begin{aligned} \Delta E_{\rm mode} &= \int dt \int d^3x \rho \mathbf{v} \cdot \nabla U = \int dt \int d^3x \rho v^i \nabla_i U \\ &\approx \int dt \int d^3x \rho \mathcal{E}_{ik}(t) \dot{\xi}^i x^k \\ &= \sum_n \int dt \mathcal{E}^{ik}(t) \dot{A}^{(n)}(t) \int d^3x \rho \xi_i^{(n)}(x) x_k. \end{aligned} \tag{7}$$

On the one hand, we note that Eq. (4) (within the quadrupole approximation) can be written as

$$\begin{aligned} \ddot{A}^{(n)} + \omega_n^2 A^{(n)} &= \int d^3x \rho \xi_i^{(n)*}(x) x_k \mathcal{E}^{ik}(t) \\ &\equiv \mathcal{O}_{ik}^* \mathcal{E}^{ik}(t) \end{aligned} \tag{8}$$

so that the change of the mode energy becomes

$$\begin{aligned} \Delta E_{\rm mode} &= \sum_n \int dt \mathcal{E}^{ik}(t) \dot{A}^{(n)}(t) \mathcal{O}_{ik} \\ &= \sum_n \int dt \dot{A}^{(n)}(t) (\ddot{A}^{(n)*} + \omega_n^2 A^{(n)*}) \\ &= \Delta \left\{ \frac{1}{2} \sum_n [|\dot{A}^{(n)}(t)|^2 + \omega_n^2 |A^{(n)}|^2] \right\}. \end{aligned} \tag{9}$$

The physical meaning of the above expression is obvious: the change in mode energy can be divided into kinetic energy change and potential energy change.

As an initial value problem, the solution of Eq. (8) is given by

$$\begin{aligned} A^{(n)}(t) = &\frac{1}{\omega_n} \int_{-\infty}^{t} dt' \sin[\omega_n (t - t')] \mathcal{E}_{ij}(t') \mathcal{O}^{ij*} \\ &+ \left(A_{\rm init}^{(n)}|_{t=0} \cos \omega_n t + \frac{\dot{A}_{\rm init}^{(n)}|_{t=0}}{\omega_n} \sin \omega_n t \right), \end{aligned} \tag{10}$$

with $A_{\rm init}^{n}(t)$ being an initial oscillation in the given mode of the star prior to any tidal interaction. Within the osculating orbit approximation, stringing together a sequence of pericenter encounters, the new tidally induced oscillation at each encounter can be modeled by an expression of the form (10), with the constants $(A_{\rm init}^{(n)}|_{t=0}, \dot{A}_{\rm init}^{(n)}|_{t=0})$ determined using the previous cycle's $A^{(n)}(t)$, appropriately damped by GW emission.

On the other hand, we can rewrite the mode evolution equation in the frequency domain, with

$$\tilde{A}^{(n)} = \frac{\langle \boldsymbol{\xi}^{(n)} | \nabla \tilde{U} \rangle}{\omega_n^2 - \omega^2} = \frac{\mathcal{O}_{ik}^* \tilde{\mathcal{E}}^{ik}}{\omega_n^2 - \omega^2}, \tag{11}$$

and

$$\chi(t) \equiv \int_{-\infty}^{\infty} d\omega \tilde{\chi}(\omega) e^{-i\omega t}. \tag{12}$$

The frequency domain equation [Eq. (11)] is suitable to describe the evolution with zero initial oscillations, e.g., in cases where the mode decay time scale is shorter than the orbital time scale. In the frequency-domain description, the energy deposited into modes is [42]

$$\Delta E_{\rm mode} = 2\pi^2 \sum_n |\mathcal{O}_{ik}^* \tilde{\mathcal{E}}^{ik}(\omega_n)|^2. \tag{13}$$

In addition to energy, part of the orbital angular momentum is also transferred to the star through the dynamical coupling between the tidal bulge and the companion star. Similar to Eq. (7), with the power injected replaced by the torque acting on each mass element, we have

$$\begin{aligned}\Delta J_{\rm mode}{}^{i} &= \int dt \int d^3x\rho\epsilon^{ijk}(x_j+\xi_j)\nabla_k U \\ &= \int dt\epsilon^{ijk}\mathcal{E}_k{}^{l}\int d^3x\rho(x_j+\xi_j)(x_l+\xi_l) \\ &\approx \int dt\epsilon^{ijk}\mathcal{E}_k{}^{l}\int d^3x\rho(x_j\xi_l+\xi_j x_l) \\ &= 2\sum_n \int dt\mathcal{E}_k{}^{l}(t)A^{(n)}(t)\int d^3x\rho\xi^{(n)}_{\langle l}(x)x_{j\rangle}\epsilon^{ijk} \\ &= 2\sum_n \int dt\epsilon^{ijk}\mathcal{E}_k{}^{l}(t)A^{(n)}(t)\mathcal{O}_{\langle jl\rangle}, \end{aligned} \tag{14}$$

with the symmetrized tensor $\mathcal{O}_{\langle jl\rangle}$ being $(\mathcal{O}_{jl}+\mathcal{O}_{lj})/2$, and in the third line we have neglected $\mathcal{O}(\xi^2)$ terms. In this study, we choose the coordinate system such that the stellar trajectory resides on the equatorial plane, and only consider the change of angular momentum along the z axis:

$$\Delta J_{\rm mode,z} = 2\sum_n \int dt(\mathcal{E}^{yl}(t)\mathcal{O}_{\langle xl\rangle} - \mathcal{O}_{\langle yl\rangle}\mathcal{E}^{xl}(t))A^{(n)}(t). \tag{15}$$

In the frequency domain, similarly to the evaluation for the mode energy, Eq. (14) can be rewritten as

$$\begin{aligned}\Delta J_{\rm mode,i} &= 4\pi\sum_n \int d\omega\tilde{\mathcal{E}}^{kl*}(\omega)\tilde{A}^{(n)}(\omega)\mathcal{O}_{\langle lj\rangle}\epsilon_{ijk} \\ &= 4\pi\sum_n \int d\omega\tilde{\mathcal{E}}^{kl*}(\omega)\mathcal{O}_{\langle lj\rangle}\epsilon_{ijk}\frac{\tilde{\mathcal{E}}^{gh}\mathcal{O}^*_{hg}}{\omega_n^2-\omega^2-i\epsilon} \\ &= \frac{4\pi^2 i}{\omega_n}\sum_n \epsilon_{ijk}[\tilde{\mathcal{E}}^{kl*}(\omega_n)\tilde{\mathcal{E}}^{gh}(\omega_n)-\tilde{\mathcal{E}}^{kl}(\omega_n)\tilde{\mathcal{E}}^{gh*}(\omega_n)] \\ &\quad\times\mathcal{O}^*_{\langle hg\rangle}\mathcal{O}_{\langle lj\rangle}, \end{aligned} \tag{16}$$

where we have used the fact that $\mathcal{E}$ is a symmetric tensor.

B. Typical orbits

The energy and angular momentum lost to mode excitations is generally smaller than that lost to GW radiation from the orbital motion. As a result, we adopt the Newtonian description of eccentric orbits when we compute the NS mode excitations. Such a simplified treatment also facilitates a direct comparison with previous work [37,42]. On the other hand, to track the long-term orbital evolution, a PN/quasi-Keplerian formalism [41] becomes necessary, which we discuss in Sec. V. In this section, we discuss marginally unbound (parabolic) and bound eccentric orbits separately.

1. Parabolic orbit

In the rest frame of a reference star, the parabolic orbit of the companion star can be parametrized by

$$\begin{aligned} r_t &= R_0(1+\tau^2), \\ t &= \left[\frac{2R_0^3}{G(M_*+M)}\right]^{1/2}(\tau+\tau^3/3), \\ \tau &= \tan\frac{\Phi}{2}, \end{aligned} \tag{17}$$

where r_t is the orbital separation, t is the time from pericenter passage, Φ is the true anomaly, M and M_* are the masses of the reference and incoming star, respectively, and R_0 is the pericenter distance. In Cartesian coordinates, the position in (x,y) (equatorial plane) is then given by

$$x = r_t\cos\Phi, \qquad y = r_t\sin\Phi. \tag{18}$$

The quadrupole tidal tensor, generated by an incoming star following the above trajectory is given by

$$\mathcal{E} = \frac{M_*}{r_t^3}\begin{bmatrix} -\frac{1}{2}-\frac{3}{2}\cos 2\Phi & \frac{3}{2}\sin 2\Phi & 0 \\ \frac{3}{2}\sin 2\Phi & \frac{-1}{2}+\frac{3}{2}\cos 2\Phi & 0 \\ 0 & 0 & 1 \end{bmatrix}. \tag{19}$$

The symmetrized overlap tensor $\mathcal{O}_{\langle\rangle}$ is given by

$$\mathcal{O}_{\langle ab\rangle} = \frac{Q^{(n)}_\xi}{2}\int d\Omega(e_{\hat{a}}\cdot e_{\hat{r}})(e_{\hat{b}}\cdot e_{\hat{r}})Y_{lm}, \tag{20}$$

with $e_{\hat{a}}$ being a unit coordinate vector, $e_{\hat{r}}$ being the unit radial vector and $Q^{(n)}_\xi$ defined as (with R_* being the radius of the star)

$$Q^{(n)}_\xi \equiv 2\int_0^{R_*} drr^3\rho(\xi^{(n)}_R + 3\xi^{(n)}_S). \tag{21}$$

The quadrupole tidal field excites NS modes with $l=2$ only. Summing over the azimuthal wave numbers of the f-modes (and neglecting contributions from p- and g-modes), in the time domain, the angular momentum shift of the star is

$$\begin{aligned}\Delta J_{\rm mode,z} &= 2\sum_{l=2,m}\int dt(\mathcal{E}^{yl}(t)\mathcal{O}_{xl} - \mathcal{O}_{yl}\mathcal{E}^{xl}(t))A^{(n)}(t) \\ &= \sqrt{6\pi/5}\int dt\frac{M_*}{r_t^3}\Big[-iQ^{22}_\xi e^{2i\Phi}A_{22}(t) \\ &\quad + iQ^{2,-2}_\xi e^{-2i\Phi}A_{2,-2}(t)\Big], \end{aligned} \tag{22}$$

where

$$A_{22} = \frac{Q_\xi^{22}}{2\omega_{22}} \int_{-\infty}^{t} dt' \sqrt{6\pi/5} \frac{M_*}{r_t^3} \sin\omega_{22}(t-t') e^{-2i\Phi(t')} + \left(A_{\rm init}^{(22)}|_{t=0} \cos\omega_{22} t + \frac{\dot{A}_{\rm init}^{(22)}|_{t=0}}{\omega_{22}} \sin\omega_{22} t \right),$$

$$A_{2,-2} = \frac{Q_\xi^{2,-2}}{2\omega_{2,-2}} \int_{-\infty}^{t} dt' \sqrt{6\pi/5} \frac{M_*}{r_t^3} \sin\omega_{2,-2}(t-t') e^{2i\Phi(t')} + \left(A_{\rm init}^{(2,-2)}|_{t=0} \cos\omega_{2,-2} t + \frac{\dot{A}_{\rm init}^{(2,-2)}|_{t=0}}{\omega_{2,-2}} \sin\omega_{2,-2} t \right). \quad (23)$$

For nonrotating stars, or if we neglect the split of oscillation modes due to rotation, we have $\omega_{22} = \omega_{2,-2}$, $Q_\xi^{l,m} = Q_\xi^{l,-m*}$ and $A_{22} = A_{2,-2}^*$:

$$\begin{aligned}\Delta J_{\rm mode,z} &= |Q_\xi^{22}|^2 \frac{3\pi}{5\omega_{22}} \int_{-\infty}^{\infty} dt \int_{-\infty}^{t} dt' \frac{M_*^2}{r_t^3 r_t'^3} \sin\omega_{22}(t-t') \times \sin[2(\Phi-\Phi')] \\ &= |Q_\xi^{22}|^2 \frac{3\pi}{10\omega_{22}} \int_{-\infty}^{\infty} dt \int_{-\infty}^{\infty} dt' \frac{M_*^2}{r_t^3 r_t'^3} \sin\omega_{22}(t-t') \times \sin[2(\Phi-\Phi')]. \end{aligned} \quad (24)$$

The energy change under the same assumption (no initial oscillation) can be obtained by using Eqs. (7) and (10):

$$\begin{aligned}\Delta E_{\rm mode} &= \sum_n \int_{-\infty}^{\infty} dt \int_{-\infty}^{t} \cos\omega_n(t-t') \mathcal{E}_{ij}(t') \times \mathcal{O}^{ij*} \mathcal{E}_{pq}(t) \mathcal{O}^{pq} \\ &= |Q_\xi^{22}|^2 \frac{3\pi}{10} \int_{-\infty}^{\infty} dt \int_{-\infty}^{\infty} dt' \frac{M_*^2}{r_t^3 r_t'^3} \cos\omega_{22}(t-t') \times \cos[2(\Phi-\Phi')] \\ &\quad + |Q_\xi^{20}|^2 \frac{\pi}{10} \int_{-\infty}^{\infty} dt \int_{-\infty}^{\infty} dt' \frac{M_*^2}{r_t^3 r_t'^3} \cos\omega_{20}(t-t'). \end{aligned} \quad (25)$$

If we define (similar to Ref. [42])

$$I_m(y) = \int_0^\infty \frac{dx}{(1+x^2)^2} \cos\left[\sqrt{2} y (x + x^3/3) + 2m \tan^{-1} x\right], \quad (26)$$

$\Delta J_{\rm mode,z}$ in Eq. (24) can be rewritten as

$$\Delta J_{\rm mode,z} = (Q_\xi^{22})^2 \frac{6\pi}{5\omega_{22}} \frac{M_*^2}{G(M+M_*)R_0^3} [I_{-2}^2(\varpi_{22}) - I_2^2(\varpi_{22})], \quad (27)$$

with the renormalized frequency ϖ given by

$$\varpi \equiv \left[\frac{R_0^3}{G(M+M_*)}\right]^{1/2} \omega. \quad (28)$$

Similarly, the energy change described by Eq. (25) can be rewritten as

$$\Delta E_{\rm mode} = (Q_\xi^{22})^2 \frac{6\pi}{5} \frac{M_*^2}{G(M+M_*)R_0^3} [I_{-2}^2(\varpi_{22}) + I_2^2(\varpi_{22})] + (Q_\xi^{20})^2 \frac{4\pi}{5} \frac{M_*^2}{G(M+M_*)R_0^3} I_0^2(\varpi_{20}). \quad (29)$$

This is consistent with the result in Ref. [42] obtained using the frequency-domain calculation.

2. Bound eccentric orbits

Although a highly eccentric bound orbit near its pericenter can be well approximated by a parabolic orbit, we still present the energy and angular momentum transfer due to mode excitations explicitly, which is relevant for an evolving sequence of encounters.

A bound ($e < 1$) eccentric orbit can be described by

$$\begin{aligned} r_t &= \frac{p_0}{1+e\cos\Phi} = a_0(1-e\cos\tau), \\ t &= \left[\frac{a_0^3}{G(M_*+M)}\right]^{1/2} (\tau - e\sin\tau), \\ \tau &= \arccos\frac{e+\cos\Phi}{1+e\cos\Phi}, \end{aligned} \quad (30)$$

where p_0 is the semilatus rectum, a_0 is the length of the semimajor axis, e is the eccentricity ($1-e \ll 1$ for highly eccentric orbits), τ is the mean anomaly, and Φ is the true anomaly. The pericenter distance R_0 equals $a_0(1-e)$. Following the same procedure as in Sec. II B 1, but with a new quantity P_m defined to replace I_m,

$$P_m(y) = \int_0^\pi \frac{dx}{(1-e\cos x)^2} \times \cos\left[y \frac{x - e\sin x}{(1-e)^{3/2}} + m\cos^{-1}\frac{\cos x - e}{1-e\cos x} \right], \quad (31)$$

the angular momentum change of the reference star after each passage is

$$\Delta J_{\rm mode,z} = |Q^{22}_{\xi}|^2 \frac{3\pi}{5\omega_{22}} \frac{M_*^2}{G(M+M_*)a_0^3} [P^2_{-2}(\varpi_{22}) - P^2_2(\varpi_{22})] + \frac{2\sqrt{6\pi/5}M_*}{a_0^{3/2}[G(M+M_*)]^{1/2}} [P_{-2}(\varpi_{22}) + P_2(\varpi_{22})] {\rm Im}[A^{(22)}_{\rm init} Q^{22}_{\xi}]$$
$$+ \frac{2\sqrt{6\pi/5}M_*}{\omega_{22} a_0^{3/2}[G(M+M_*)]^{1/2}} [P_{-2}(\varpi_{22}) - P_2(\varpi_{22})] {\rm Re}[\dot{A}^{(22)}_{\rm init} Q^{22}_{\xi}], \tag{32}$$

where we no longer ignore the residual oscillation from previous encounters during a series of pericenter passages. Similarly the modal energy change is

$$\Delta E_{\rm mode} = |Q^{22}_{\xi}|^2 \frac{3\pi}{5} \frac{M_*^2}{G(M+M_*)a_0^3} [P^2_{-2}(\varpi_{22}) + P^2_2(\varpi_{22})] + |Q^{20}_{\xi}|^2 \frac{2\pi}{5} \frac{M_*^2}{G(M+M_*)a_0^3} P^2_0(\varpi_{20})$$
$$+ \frac{\omega_{22}\sqrt{6\pi/5}M_*}{a_0^{3/2}[G(M+M_*)]^{1/2}} [P_{-2}(\varpi_{22}) - P_2(\varpi_{22})] {\rm Im}[A^{(22)}_{\rm init} Q^{22}_{\xi}]$$
$$+ \frac{\sqrt{6\pi/5}M_*}{a_0^{3/2}[G(M+M_*)]^{1/2}} [P_{-2}(\varpi_{22}) + P_2(\varpi_{22})] {\rm Re}[\dot{A}^{(22)}_{\rm init} Q^{22}_{\xi}] - \frac{2\sqrt{\pi/5}M_*}{a_0^{3/2}[G(M+M_*)]^{1/2}} \dot{A}^{(20)}_{\rm init} Q^{20}_{\xi} P_0(\varpi_{20}). \tag{33}$$

C. Mode damping

Soon after each periastron passage, the distance between the stars grows large enough so that the tidal interaction is no longer important until the next periastron passage. Therefore we shall approximate the mode evolution between two periastron passages as free evolution damped by GW radiation. The mode damping due to viscosity is expected to have a time scale longer than the time scales such systems would remain in the aLIGO band (or future ground-based detectors such as Einstein Telescope and Cosmic Explorer), and shall be neglected in this analysis.

The mode damping due to GW radiation can be approximated using the quadrupole formula:

$$\frac{dE_{\rm mode}}{dt} = -\frac{1}{5} \left\langle \frac{\partial^3 \mathcal{I}_{jk}}{\partial t^3} \frac{\partial^3 \mathcal{I}_{jk}}{\partial t^3} \right\rangle_t, \tag{34}$$

where $\langle\rangle_t$ is the temporal average (over time scales longer than the oscillation period but shorter than the decay time) and the trace-free quadrupole moment is

$$\mathcal{I}_{jk} = \int d^3x \rho \left(x_j x_k - \frac{\delta_{jk}}{3} r^2 \right). \tag{35}$$

Because the fluid motion following the f-mode eigenfunction is trace-preserving for the quadrupole moment, the r^2 term in Eq. (35) can be dropped, so we have

$$\dddot{\mathcal{I}}_{jk} \approx \int d^3x \rho (x_j \dddot{\xi}_k + x_k \dddot{\xi}_i), \tag{36}$$

where the $\mathcal{O}(\xi^2)$ terms are neglected. We shall rewrite Eq. (34) as

$$\frac{dE_{\rm mode}}{dt} \approx -\frac{4}{5} \sum_n \left\langle \dddot{\mathcal{O}}^{(n)}_{\langle ab\rangle} \dddot{\mathcal{O}}^{(n)}_{\langle ab\rangle} |A^{(n)}|^2 \right\rangle_t. \tag{37}$$

During this "free" (without tidal driving) evolution phase, the energy damping rate is proportional to the mode amplitude squared, and the mode energy is also proportional to its amplitude squared. As a result, the mode evolution can be modeled as a decaying oscillation with a fixed quality factor Q_{lm} or decay rate $\gamma_{lm} = \pi f_{\rm mode}/Q_{lm}$. If a family of modes is initially excited, they should decay independently following their own decay rates because modes with different l, m do not overlap in angular directions (the angular average is zero), and modes with the same l, m but different overtones do not overlap in time (the temporal average is zero). For our purpose we mainly focus on $\ell = 2$ modes, as they are the dominant modes excited after the periastron passage.

Consider a decaying oscillation of the (2,2) mode

$$A^{22}(t) = \mathcal{A}^{22}(t) e^{-i\omega_{22}t} = \mathcal{A}^{22}_0 e^{-i\omega_{22}t - \gamma_{22}t} e^{i\phi_0}. \tag{38}$$

The mode energy, according to Eq. (9) (assuming $Q_{22} \gg 1$), is

$$E_{\rm mode} = \omega_{22}^2 [\mathcal{A}^{22}(t)]^2. \tag{39}$$

The right-hand side of Eq. (37) is given by

$$-\frac{4}{5} \left\langle \dddot{\mathcal{O}}_{\langle ab\rangle} \dddot{\mathcal{O}}_{\langle ab\rangle} \right\rangle_t = -\frac{1}{5} \left[Q^{(22)}_{\xi} \right]^2 \times \frac{8\pi}{15} \omega_{22}^6 [\mathcal{A}^{22}(t)]^2. \tag{40}$$

Combining Eqs. (40) and (39), we deduce the decay rate of the (2,2) mode to be

$$\gamma_{22} = \frac{4\pi}{75} \left[Q^{(22)}_{\xi} \right]^2 \omega_{22}^4, \tag{41}$$

and correspondingly the quality factor is

$$Q_{22} = \frac{75}{8\pi}[Q_\xi^{(22)}]^{-2}\omega_{22}^{-3}. \tag{42}$$

III. PARABOLIC ORBITS OF POLYTROPIC STARS

In this section, we apply the formalism presented in Sec. II to polytropic stars undergoing parabolic encounters, which allows us to compare the results with the full numerical solutions described in Sec. IV. We find that the total mode energy deposited onto stars can be comparable to the energy radiated by GWs ($\Delta E_{\rm GW}$) during a close encounter. Given the various approximations employed in the analytic treatment, we do not expect exact agreement. Better agreement may be achieved by incorporating a PN treatment of the stars' oscillation and a higher-order PN description of the orbit.

A. Prediction for polytropic EOS

To enable a simple comparison between the formalism in Sec. II and numerical simulations, we assume an equal-mass NS binary $M = M_*$, and a polytropic NS EOS, specifically $P = K\rho^\Gamma$ with $\Gamma = 2$. For such stars, the spherically symmetric equilibrium configuration can be obtained by solving

$$\begin{aligned} P'(r) &= -\rho(r)U'(r), \\ U''(r) + \frac{2U'(r)}{r} &= 4\pi G\rho(r), \end{aligned} \tag{43}$$

with U being the Newtonian potential. The corresponding solutions are

$$\begin{aligned} \rho(r) &= \rho_c \frac{\sin(\pi r/R_*)}{\pi r/R_*}, \\ P(r) &= K\left(\rho_c \frac{\sin(\pi r/R_*)}{\pi r/R_*}\right)^2, \\ U(r) &= -\frac{GM}{R_*} - 4\pi G\rho_c R_*^2 \frac{\sin(\pi r/R_*)}{\pi r/R_*}, \end{aligned} \tag{44}$$

with $K = 2GR_*^2/\pi$ and $M = 4\rho_c R_*^3/\pi$. Both K and ρ_c are fixed if we choose the NS radius for a given NS mass. According to the analysis in the Appendix, the normalized f-mode eigenfrequencies for such stars are given by

$$\varpi_{20} = \varpi_{2,\pm2} = 0.8676\left(\frac{R_0}{R_*}\right)^{3/2}. \tag{45}$$

The frequency degeneracy is due to the spherical symmetry of the background solution, such that the mode frequency is independent of the azimuthal wave number. Similarly, the mode overlap constants for the (2,2) and (2,0) modes are the same, as $\xi_R^{(n)}$ and $\xi_S^{(n)}$ are also independent of m due to the spherical symmetry [the (2,1) mode is irrelevant for computing energy and angular momentum transfer, according to Eqs. (29) and (27)]. The detailed form of the radial dependence of wave functions can be obtained using the method described in the Appendix. The overlap constants are

$$Q_\xi^{22} = Q_\xi^{20} = 0.558(MR_*^2)^{1/2}, \tag{46}$$

which implies that the quality factors [cf. Eq. (42)] are

$$Q_{2,\pm2} = Q_{20} \approx 5.2\left(\frac{R_*}{M}\right)^{5/2}. \tag{47}$$

From Eqs. (45) and (26), the mode excitation coefficients (as functions of R_0/R_*) are shown in Fig. 1. Notice that under the convention in Eq. (26), the magnitude of I_{-2} is much greater than I_2, which has to do with the fact that the star's motion is counterclockwise as described by Eq. (17). As a result, when we use Eq. (29) to compute the mode energy, the $m = -2$ piece dominates over other parts. Note that the authors of Ref. [21] claimed that the $m = -2$ mode therein is negligible, so that the study in Ref. [37] only included the $m = 2$ piece, which turns out to be subdominant in the modes excited. This is because the amplitude of $m = 2$ mode in Ref. [21] was the same as the $m = -2$ mode in Ref. [42] due to the different conventions used. Once we include all mode pieces (especially the $m = -2$ piece), the result becomes consistent with the values inferred by numerical simulations.

With the excitation coefficients shown in Fig. 1, and the overlap constants obtained from Eq. (46), we can write the mode energy in Eq. (29) as

$$\begin{aligned} \Delta E_{\rm mode} = {} & 0.587\frac{GM^2R_*^2}{R_0^3}[I_{-2}^2(\varpi_{22}) + I_2^2(\varpi_{22})] \\ & + 0.391\frac{GM^2R_*^2}{R_0^3}I_0^2(\varpi_{20}), \end{aligned} \tag{48}$$

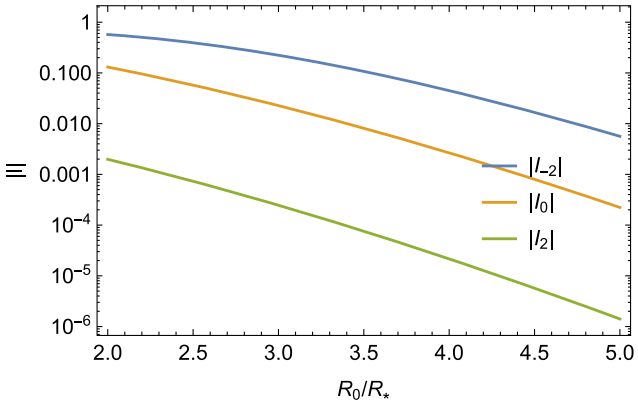

FIG. 1. $|I_{\pm2}|$ and $|I_0|$ [Eq. (26)] as functions of R_0/R_*. In the Newtonian limit, when $R_0 = 2R_*$ the surfaces of two undeformed stars are in marginal contact at the periastron passage.

and mode angular momentum is

$$\Delta J_{\rm mode} = 0.478 \frac{G^{1/2} M^{3/2} R_*^{7/2}}{R_0^3} [I^2_{-2}(\varpi_{22}) - I^2_2(\varpi_{22})]. \quad (49)$$

Without considering mode excitations, the GW energy emitted during a periastron passage can be estimated as [37,45]

$$\Delta E_{\rm GW} \approx 7\pi \frac{(GM)^{7/2} M}{c^5 R_0^{7/2}}, \quad (50)$$

and the angular momentum carried away by GWs is

$$\Delta J_{\rm GW} \approx 6\pi \frac{(GM)^3 M}{c^5 R_0^2}. \quad (51)$$

As a result, the ratio between the mode energy deposited into both stars and the energy carried away by GWs during the main burst is

$$\frac{2\Delta E_{\rm mode}}{\Delta E_{\rm GW}} \approx \left(\frac{GM}{c^2 R_*}\right)^{-5/2} \left(\frac{R_0}{R_*}\right)^{1/2} \times 2 \times 10^{-2} \times \{2.69[I^2_{-2}(\varpi_{22}) + I^2_2(\varpi_{22})] + 1.78 I^2_0(\varpi_{20})\}. \quad (52)$$

Similarly, the ratio between the mode angular momentum deposited into both stars and the angular momentum carried away by GWs during the main burst is

$$\frac{2\Delta J_{\rm mode}}{\Delta J_{\rm GW}} \approx \left(\frac{GM}{c^2 R_*}\right)^{-5/2} \left(\frac{R_0}{R_*}\right)^{-1} \times 0.05 \times \{[I^2_{-2}(\varpi_{22}) - I^2_2(\varpi_{22})])\}. \quad (53)$$

The dominant contribution comes from the $m = -2$ mode with our conventions. As a concrete example, take a NS with compaction $GM/(c^2 R_*) \sim 0.17$ (e.g., $M \approx 1.4\, M_\odot$ and $R_* \approx 12$ km). In Fig. 2 we plot the ratio described in Eqs. (52) and (53) as a function of the "periastron frequency" f (of the orbit, and hence half the GW frequency). This frequency was introduced in Refs. [37,38] (and also discussed in Sec. IV), and represents the peak frequency of the main burst. In the Newtonian limit, f is proportional to $R_0^{-1.5}$. In Fig. 2, $f_c := \sqrt{M/(2R_*)^3}/\pi$ denotes the periastron frequency for the closest possible passage without the stars colliding. For comparison, in this figure we also show results from the full numerical solutions described in Sec. IV. These agree with the model to within a factor of 2, even at the relativistic velocities considered. The plot shows that, for very close pericenter passages, the mode energy/angular momentum deposited into the stars can be of the same order of magnitude as the energy/angular momentum carried away by GWs. This means that it is crucial to include the mode dynamics in order to accurately model the orbital evolution.

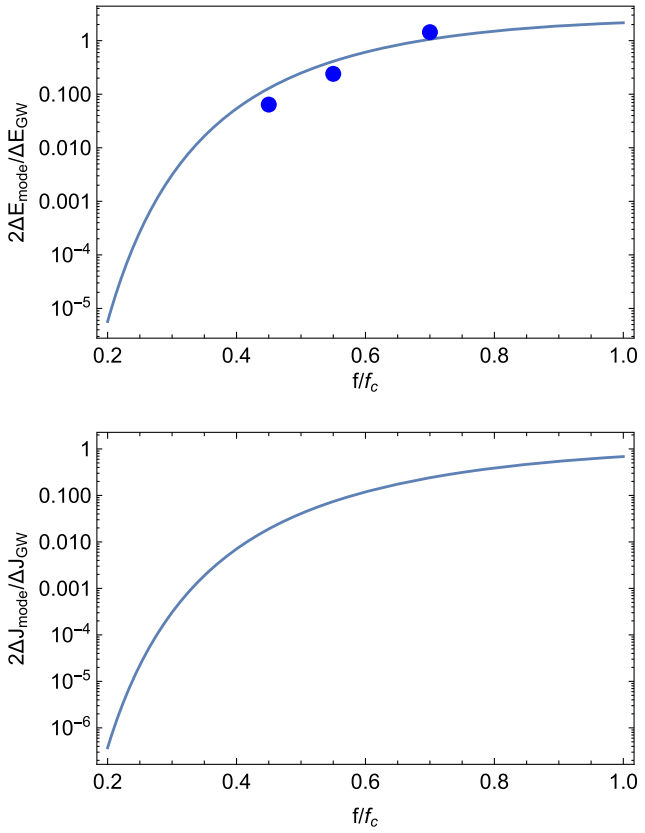

FIG. 2. The ratio between the total mode energy (angular momentum) deposited onto stars and the energy (angular momentum) carried away by GWs during the main burst, as a function of the normalized periastron frequency f/f_c. Here $R_* c^2/(GM)$ is taken to be 5.88. The dots shown in the top plot represent estimates from the numerical simulations listed in Table I.

IV. SIMULATIONS IN FULL GENERAL RELATIVITY

In order to validate the model described in the previous section, and determine its accuracy in the relativistic regime, we simulate several cases consisting of compact object binaries undergoing a close encounter using general relativity (GR) coupled to hydrodynamics. This work makes use of methods similar to those in previous studies of eccentric binary mergers [23,24,46–48], which we just briefly review here.

A. Numerical methods

These simulations are carried out by solving the full Einstein equations coupled to hydrodynamics using the methods described in Ref. [49]. For ease of comparison to the approximate model described in this work, we restrict ourselves to a $\Gamma = 2$ EOS. We make use of adaptive mesh

refinement with seven levels of refinement. The base-level resolution has 201^3 points, while the finest-level resolution has approximately 100 points across the NS diameter. For simulations with BHs, we use one additional mesh refinement level, which gives a factor of 2 better resolution, around the BH. For one of the NS-NS cases, we also perform a lower-resolution simulation with 0.6× the above resolution, in order to estimate the truncation error.

B. Initial data and cases

We study binary NS close encounters with several different impact parameters, and then follow the oscillations in the stars during the long outgoing part of the elliptic orbit. For comparison, we also consider an equal-mass BH-NS case with a nonspinning BH and the same orbital parameters as one of the binary NS cases. Initial data is constructed using the methods described in Ref. [50]. We choose the initial velocities and positions of the compact objects at large separation ($d = 50M_{\rm tot}$, where $M_{\rm tot}$ is the total mass of the system) based on a marginally bound Newtonian orbit with a specified periapse distance R_0. The actual periapse distance of the binary will be different (due to gauge effects, relativistic corrections, etc.), and we fix the parameters used for comparing to the approximate model based on the frequency of the fly-by gravitational waveform. This allows a largely gauge-invariant comparison with the model we presented in the previous section. We consider several equal-mass binary NS cases with $R_0/M_{\rm tot} = 10.0$, 11.5, and 13. For the comparison to an equal-mass BH-NS system, we use a single NS case with $R_0/M_{\rm tot} = 11.5$. In all cases we choose a NS with $M_*/R_* = 0.17$.

C. Results

In Fig. 3 we show a comparison of the GWs from a NS-NS and BH-NS case with the same orbital parameters. The fly-by part of the waveform matches well between the two cases, indicating that the incoming orbits are very close. The peak instantaneous GW frequency, calculated from the time derivative of the phase of the (2,2) component of Ψ_4 is $\omega M_{\rm tot} = 0.11$, and differs by $< 1\%$ in the two cases. This corresponds to a normalized periastron frequency of $f/f_c = 0.55$. The amount of energy radiated in GWs around the periapse passage is $\Delta E_{\rm GW}/M_{\rm tot} \approx 6.4 \times 10^{-4}$.

After the fly-by there are high-frequency GW oscillations in both cases. By going to the frequency domain we can see these GW oscillations are primarily at the expected f-mode frequency, and that the amplitude in the binary NS case is twice that of the BH-NS case, indicating that to a good approximation the stars are tidally perturbed by the same amount. In the middle panel of Fig. 3, one can see a lower-frequency modulation in the GW signal. The fact

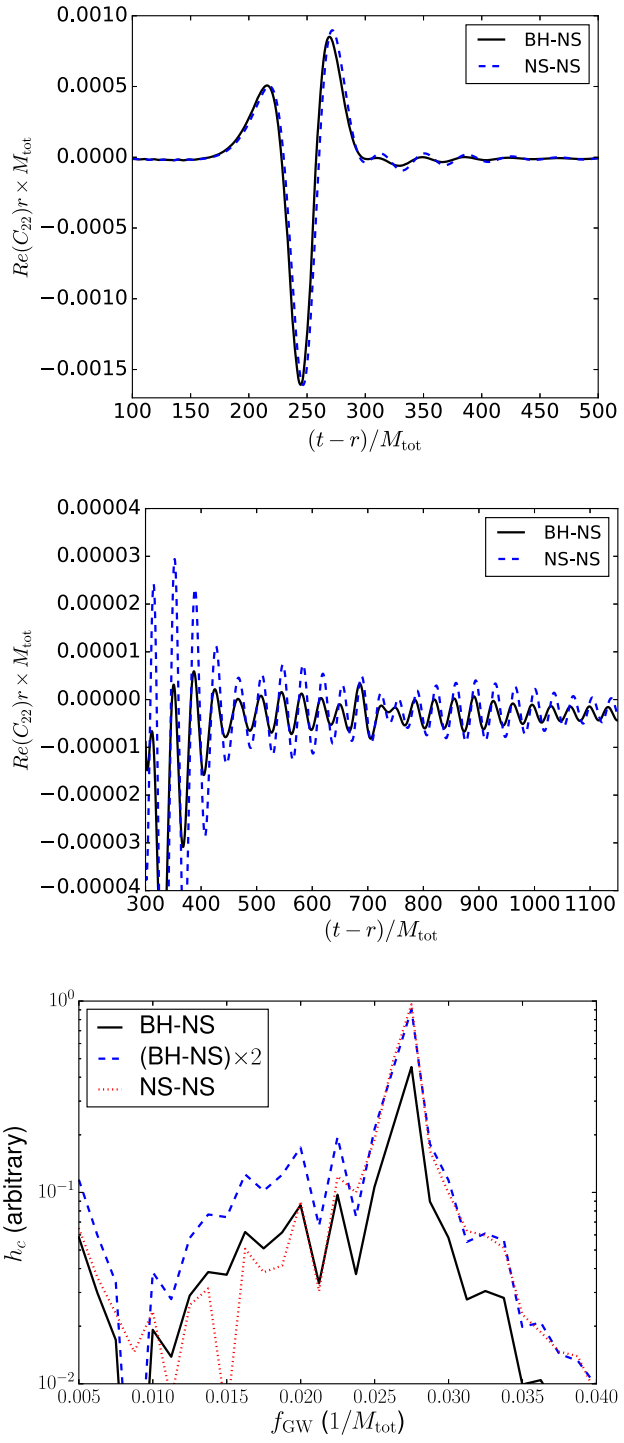

FIG. 3. A comparison of the GWs from a BH-NS and NS-NS case with $R_0/M_{\rm tot} = 11.5$. The top and middle panels show the real part of the (2,2) component of Ψ_4, the former emphasizing the GW burst from the close encounter, and the latter emphasizing the GW oscillations from the f-mode excitations in the NS(s). The bottom panel shows the post fly-by GWs ($t - r > 500M_{\rm tot}$) in the frequency domain. The peak at approximately $f_{\rm GW} \approx 0.027/M_{\rm tot}$ associated with the f-mode oscillations is a factor of 2 larger in the binary NS case, as expected if the NSs are tidally perturbed by the same amount in both cases.

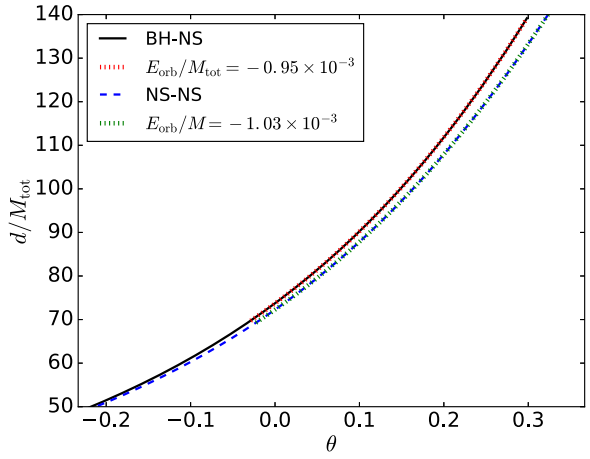

FIG. 4. The coordinate separation versus orbital angle at large distances post-fly-by for a BH-NS and NS-NS system with the same initial binary parameters. We also show the Newtonian orbits with the best-fit parameters for these two cases.

that this occurs in both the binary NS and BH-NS cases indicates that it is not due to interference effects, and is likely instead due to the spherical harmonic mode mixing at the extraction sphere.[2]

We can estimate the amount of energy lost to tidal excitations by comparing the orbits in the two cases. In Fig. 4 we show the coordinate separation of the binary as a function of angle, at large values post-fly-by. Fitting this to a Newtonian orbit, and taking the difference of the resulting values for the orbital energy for the BH-NS and NS-NS cases and attributing it to the energy of the tidal excitations in a single star gives $\Delta E_{\rm mode}/\Delta E_{\rm GW} = 0.13$.[3] In comparison, the analytic model predicts $\Delta E_{\rm mode}/\Delta E_{\rm GW} = 0.22$.

We use the above estimate of $\Delta E_{\rm mode}$ as a reference value, and also consider how the tidal excitation compares as a function of impact parameter—or equivalently, periastron frequency—for a higher and lower case. The results are summarized in Table I. All cases show the expected peak in the characteristic strain at the f-mode frequency as in the bottom panel of Fig. 3, and here we have estimated $\Delta E_{\rm mode}$ by assuming that it is proportional to the strain within this peak (within 10% of the f-mode frequency), and using the above comparison to the BH-NS to fix the overall magnitude. We also note that by comparing two different resolutions for the largest impact parameter (lowest value of the f/f_c case), and assuming second-order convergence,[4] we estimate that the truncation error in the calculation of $\Delta E_{\rm mode}$ is ∼20% (which is an underestimate), while the truncation errors in f/f_c and $E_{\rm GW}$ are smaller, $\lesssim$1%. Likely more significant are systematic effects in estimating orbital energy based on comparing coordinate trajectories for the BH-NS and NS-NS cases, and measuring tidal excitations based on the GW emission. Since our main purpose here is to establish the rough accuracy of the analytic model for tidal excitations, we leave a more in-depth study of this to future work.

TABLE I. The first two columns are the characteristic frequency and energy emitted in GWs during pericenter passage. The last two columns are an estimate of the amount of energy deposited in tidal excitations (per star) from three equal-mass, nearly parabolic binary NS encounters from the full GR calculation and the analytic model.

f/f_c	$\Delta E_{\rm GW}/M_{\rm tot}$	$\Delta E_{\rm mode}/\Delta E_{\rm GW}$ (sims.)	(model)
0.70	15.0×10^{-4}	0.72	0.53
0.55	6.4×10^{-4}	0.12	0.22
0.45	3.4×10^{-4}	0.032	0.06

Finally, we note that in these simulations and throughout we neglected tidal heating due to nonideal matter effects. Our simulations show that the bulk of the stellar interior remains cold: the thermal energy during close encounters is universally below 1% of the total internal energy. On the other hand, any tidal deformations will be dissipated into heat by nonideal effects on secular time scales, which are much longer than the dynamical time scales considered here. In particular, the thermal conduction and shear viscosity time scales are $\sim 10^8$ s [52]. The bulk viscosity time scale sensitively depends on the matter temperature (see Fig. 7 in Ref. [53]), which for cold neutron stars $T \lesssim 1$ MeV as in our cases, is much longer than seconds. Therefore, thermal effects in the bulk of the matter are negligible in these fly-by encounters. While there could be important thermal effects associated with crust cracking, a study of such phenomena goes beyond the scope of this paper.

V. TRAJECTORY MODEL

A trajectory and waveform model for highly eccentric, binary BH systems was developed in Ref. [38]. The key idea is to divide the whole trajectory into a series of PN elliptical orbits attached by a change of orbital parameters that occurs during the pericenter passage process. The shift of orbital eccentricity and energy/angular momentum can

[2]Private communication with Nathan Johnson-McDaniel. See Ref. [51].

[3]Our method of constructing initial data and resolving the constraints causes the orbital energy of the binary to be slightly negative. If instead of using the difference between the BH-NS and the NS-NS cases, one just used the orbital energy estimate for the NS-NS case, and assumed it was initially zero before the close encounter, we would have obtained a somewhat larger value of $\Delta E_{\rm mode}/\Delta E_{\rm GW} = 0.3$.

[4]Our code is second-order convergent when shocks are absent. See Ref. [24] for convergence results for eccentric binary NS encounters at numerical resolutions that closely match those used here.

be obtained by computing the accumulated GW flux within each cycle.

Based on a PN description of the orbital evolution, the BH waveform model then contains four physical quantities: $t_i, \delta t_i, f_i, \delta f_i$ for the ith cycle. Here t_i is the coordinate time for the ith periastron passage while f_i is the "periastron frequency," defined as [38]

$$f_i \equiv \frac{1}{2\pi\tau_{\rm GW}} \equiv \frac{1}{2\pi}\frac{\text{pericenter velocity}}{\text{pericenter distance}}, \tag{54}$$

which reduces to

$$f_i = \frac{1}{2\pi}\frac{[(M+M_*)(1+e)]^{1/2}}{R_0^{3/2}} \tag{55}$$

in the Newtonian limit.

Phenomenologically, $2f_i$ well approximates the central burst frequency of GWs corresponding to the ith periastron passage. With the predictions of t_i and f_i for the central arriving time and frequency of each GW burst, one can extract a sequence of centroids of size $\delta t_i \times \delta f_i$ in the time-frequency diagram around (t_i, f_i), compute the spectrum within each centroid, and possibly stack the spectra power of different centroids to boost the total signal-to-noise ratio [15,54]. The choices for δt_i and δf_i are rather flexible; in Ref. [38] they were chosen to be constant multiples of $\tau_{\rm GW}$ and f_i.

We notice that if the orbital evolution and GW emission can be modeled with enough accuracy, such that the phase error of the waveform for the whole duration is controlled within $\mathcal{O}(1/\mathrm{SNR})$ (with SNR being the signal-to-noise ratio of a typical event), it is preferable to use a single waveform covering the whole duration for both detection and parameter estimation purposes. This requirement is challenging because the binary dynamics could be quite nonlinear near pericenter passages, and the total duration could contain many cycles. It is computationally prohibitive to perform numerical simulations of this type to calibrate the theoretical waveforms designed for such systems. Nevertheless, one possibility is to use a waveform calibrated by numerical relativity when the NSs are close to each other, and then match it to a PN waveform when the two stars are far apart. We shall leave further investigation of this to future work.

A. Order-of-magnitude estimates

As discussed in Sec. III, and explicitly shown in Fig. 2, the energy/angular momentum deposited into the stars may be of the same order of magnitude as the energy/angular momentum carried away by GWs during close pericenter passages. In this case it is necessary to include the effect of mode excitations in the evolution model for such orbits.

To quantify the regime of importance for mode excitations, we notice that $2\Delta E_{\rm mode}/\Delta E_{GW}$ in Fig. 2 exceeds 1% only when $f/f_c \geq 1/3$, which means that

$$f \geq \frac{f_c}{3} \sim 3.9\times 10^2\ \mathrm{Hz}\left(\frac{M}{1.4\ M_\odot}\right)^{1/2}\left(\frac{R_*}{12\ \mathrm{km}}\right)^{-3/2}. \tag{56}$$

Another question is whether it is necessary to include the oscillations inherited from the previous pericenter passage as in Eqs. (33) and (32), instead of setting $A_{\rm init}$ and $\dot{A}_{\rm init}$ to zero before each pericenter passage. To answer this question, we compare the mode decaying time scale $1/\gamma_{22}$ with the orbital period (in the Newtonian limit)

$$\begin{aligned} T &= 2\pi\left[\frac{G(M+M_*)}{a_0^3}\right]^{-1/2} \\ &= 2\pi\left[\frac{G(M+M_*)}{R_0^3}\right]^{-1/2}(1-e)^{-3/2}. \end{aligned} \tag{57}$$

We conclude that the initial oscillations are negligible if (assuming $M = M_*$)

$$1-e \ll 0.63\frac{R_0}{R_*}\left(\frac{GM}{R_* c^2}\right)^{5/3}. \tag{58}$$

If we consider the type of NS assumed to produce Fig. 2 and consider the closest passage with $R_0 = 2R_*$, the above inequality can be translated to $1-e \ll 0.07$. For such binaries [with Eq. (58) satisfied], it is no longer necessary to track the evolution of modes, as the lifetime of the modes is smaller than the time between pericenter passages. However, in order to compute the energy and angular momentum change of the orbit after pericenter passages, it is still necessary to include the mode contributions using Eqs. (33) and (32), with $A_{\rm init}$ and $\dot{A}_{\rm init}$ set to zero.

In the special case studied in Sec. IV, the two NSs are assumed to be identical, which means that their f-modes have the same frequency. The GWs generated by f-mode oscillations from two stars may beat with each other, depending on the separation of two stars and the sky direction of observers. This beating starts to become important if the orbital separation is comparable to, or larger than, the half-wavelength of the f-mode GWs:

$$1 \leq \frac{a_0(1+e)}{\lambda/2} \approx \frac{2R_0\omega_{22}}{\pi(1-e)c}, \tag{59}$$

or equivalently

$$1-e \leq 0.78\frac{R_0}{R_*}\left(\frac{GM}{R_* c^2}\right)^{1/2}. \tag{60}$$

In reality, the masses of individual NSs within the binary will be different (we denote the mass difference as $\Delta M = M - M_*$). According to the f-mode frequency formula [see Eq. (45)], we have $\delta f/f \sim 0.5\Delta M/M$. The beating generally loses constructive interference after $f/2\delta f \sim M/\Delta M$ oscillation cycles.

B. Trajectory model

The quasi-Keplerian (QK) description of eccentric orbits of a compact binary was well explained in Ref. [41]. In this framework, the 1PN motion of the binary in the radial, time, and angular directions can be written in the following form:

$$\begin{aligned} r &= a_r(1 - e_r \cos u), \\ \ell &= u - e_t \sin u + \mathcal{O}(c^{-4}), \\ \frac{\phi - \phi_p}{K} &= v + \mathcal{O}(c^{-4}) = 2\arctan\left[\left(\frac{1+e_\phi}{1-e_\phi}\right)^{1/2}\tan\frac{u}{2}\right], \end{aligned} \tag{61}$$

where v is the true anomaly, u is the eccentric anomaly, $\ell = n(t - t_p)$ is the mean anomaly with $n = 2\pi/T$ being the mean motion, and P is the period. In addition, K is related to the periastron precession angle per cycle $\Delta\phi_p$ by $\Delta\phi_p = 2\pi(K-1)$. The above QK representation has been generalized to 2PN [55–57] and 3PN orders [58]. The orbital eccentricities e_t, e_r, and e_ϕ, and additional parameters n, K, and a_r are all functions of the orbital energy and angular momentum [see Eq. (345) in Ref. [41]], and we introduce a new set of parameters to match the convention in Ref. [41]:

$$\epsilon = -\frac{2E}{\mu c^2}, \qquad j = -\frac{2Eh^2}{\mu^3}, \tag{62}$$

with $\mu = (M + M_*)\nu$, $\nu = MM_*/(M+M_*)^2$ and $h = J/G(M+M_*)$. In order to obtain a mapping for orbital parameters from one cycle to the next, we first compute the energy and angular momentum change within the current cycle:

$$\begin{aligned} E_{i+1} &= E_i + \Delta E_{\mathrm{GW,i}} + \Delta E_{\mathrm{mode,i}}, \\ J_{i+1} &= J_i + \Delta J_{\mathrm{GW,i}} + \Delta J_{\mathrm{mode,i}}. \end{aligned} \tag{63}$$

The energy and angular momentum radiated by the orbital motion within the ith cycle are

$$\begin{aligned} \Delta E_{\mathrm{GW,i}} &= \langle \dot{E}_{\mathrm{GW,i}} \rangle T_i = \langle \dot{E}_{\mathrm{GW,i}} \rangle \frac{2\pi}{n_i}, \\ \Delta J_{\mathrm{GW,i}} &= \langle \dot{J}_{\mathrm{GW,i}} \rangle \frac{2\pi}{n_i} \end{aligned} \tag{64}$$

where n_i is given by Eq. (347a) in Ref. [41]. The 3PN orbital-averaged energy flux can be obtained from Eq. (355) in Ref. [41], and the 3PN averaged angular momentum can be found in Ref. [59]. For the mode energy and angular momentum change we use Eqs. (33), (32), and (62). There is however one subtlety, which is to include the residual oscillation from the previous pericenter passage in the calculation, i.e., the terms involving A_{init} and $\dot{A}_{\mathrm{init}}$. Based on Eq. (23), we denote $A_{\mathrm{init,i}} = A_{\mathrm{init}}(t_i), \dot{A}_{\mathrm{init,i}} = \dot{A}_{\mathrm{init}}(t_i)$, and explicitly write down their mapping relations as (with $Q \gg 1$)

$$\begin{aligned} A^{22}_{\mathrm{init,i+1}} &= \left[A^{22}_{\mathrm{init,i}} + i\sqrt{3\pi/10}\frac{M_*}{na_r^3}Q_\xi(P_{-2} - P_2)\right]\left[\cos(\omega T_i) + \frac{\gamma}{\omega}\sin(\omega T_i)\right]e^{-\gamma T_i} \\ &\quad + \left[\sqrt{3\pi/10}\frac{M_*}{na_r^3}Q_\xi(P_{-2} + P_2) + \dot{A}^{22}_{\mathrm{init,i}}\right]\frac{\sin(\omega T_i)}{\omega}e^{-\gamma T_i}, \\ \dot{A}^{22}_{\mathrm{init,i+1}} &= \left[\sqrt{3\pi/10}\frac{M_*}{na_r^3}Q_\xi(P_{-2} + P_2) + \dot{A}^{22}_{\mathrm{init,i}}\right]\left[\cos(\omega T_i) - \frac{\gamma}{\omega}\sin(\omega T_i)\right]e^{-\gamma T_i} \\ &\quad - \left[A^{22}_{\mathrm{init,i}} + i\sqrt{3\pi/10}\frac{M_*}{na_r^3\omega}Q_\xi(P_{-2} - P_2)\right]\omega\sin(\omega T_i)e^{-\gamma T_i}, \end{aligned} \tag{65}$$

with $A^{22}_{\mathrm{init,i}} = A^{2,-2*}_{\mathrm{init,i}}$, $\dot{A}^{22}_{\mathrm{init,i}} = \dot{A}^{2,-2*}_{\mathrm{init,i}}$ and similarly

$$\begin{aligned} A^{20}_{\mathrm{init,i+1}} &= A^{20}_{\mathrm{init,i}}\left[\cos(\omega T_i) + \frac{\gamma}{\omega}\sin(\omega T_i)\right]e^{-\gamma T_i} + \left[-\sqrt{4\pi/5}\frac{M_*}{na_r^3}Q_\xi P_0 + \dot{A}^{20}_{\mathrm{init,i}}\right]\frac{\sin(\omega T_i)}{\omega}e^{-\gamma T_i}, \\ \dot{A}^{20}_{\mathrm{init,i+1}} &= \left[-\sqrt{4\pi/5}\frac{M_*}{na_r^3}Q_\xi P_0 + \dot{A}^{20}_{\mathrm{init,i}}\right]\left[\cos(\omega T_i) - \frac{\gamma}{\omega}\sin(\omega T_i)\right]e^{-\gamma T_i} - A^{20}_{\mathrm{init,i}}\omega\sin(\omega T_i)e^{-\gamma T_i}, \end{aligned} \tag{66}$$

where we have abbreviated the mode index for frequencies and decay rates because they are the same for all modes with $\ell = 2$.

In reality, even if the initial mode oscillation is known at the beginning of a sequence of bursts, the phase error due to the PN approximation and the osculating orbit approximation may accumulate with time and eventually lead to very inaccurate predictions for A_{init} and $\dot{A}_{\mathrm{init}}$. As a result, if we denote the time for a template to receive an $\mathcal{O}(1)$ phase error as τ_1, an accurate template should satisfy $\tau_1\gamma_{22} > 1$.

To 1PN order, the periastron frequency of the ith cycle f_i is given by [38]

$$f_i \equiv \frac{1}{2\pi}\frac{\text{pericenter velocity}}{\text{pericenter distance}} = \frac{1}{2\pi}\sqrt{\frac{1+e_\phi}{1-e_\phi}}\frac{nK}{1-e_t}. \tag{67}$$

At 3PN order, f_i can be obtained by combining Eqs. (346) and (343) in Ref. [41]:

$$\begin{aligned} f_i &= \frac{n}{2\pi}\frac{d\phi/du}{d\ell/du} = \frac{nK}{2\pi}\frac{dv}{du}\bigg|_{u=0}\frac{1+2f_\phi\cos 2v+3g_\phi\cos 3v+4i_\phi\cos 4v+5h_\phi\cos 5v}{1-e_t\cos u-g_t+dv/du(g_t+f_t\cos v+2i_t\cos 2v+3h_t\cos 3v)}\bigg|_{u,v=0} \\ &= \frac{nK}{2\pi}\sqrt{\frac{1+e_\phi}{1-e_\phi}}\frac{1+2f_\phi+3g_\phi+4i_\phi+5h_\phi}{1-e_t-g_t+\sqrt{\frac{1+e_\phi}{1-e_\phi}}(g_t+f_t+2i_t+3h_t)}, \end{aligned} \tag{68}$$

where the definitions of and more discussions on the orbital elements f_ϕ, g_ϕ, i_ϕ, h_ϕ, f_t, g_t, i_t, h_t, e_t, e_r, e_ϕ can be found in Refs. [41,58].

Under the impulsive approximation, the Newtonian formula for the energy and angular momentum deposited into the stars, i.e., Eqs. (33) and (32), can be further improved by incorporating the 1PN trajectory description in Eq. (61). To do that, we only need to replace a_0 in Eqs. (32) and (33) by a_r, and the definition of $P_m(y)$ by

$$\begin{aligned} P_m(y) = \int_0^\pi \frac{dx}{(1-e_r\cos x)^2}\cos\Bigg\{ y\frac{x-e_t\sin x}{n} \\ + 2mK\arctan\left[\left(\frac{1+e_\phi}{1-e_\phi}\right)^{1/2}\tan\frac{u}{2}\right]\Bigg\}, \end{aligned} \tag{69}$$

and $\Delta E_{\rm mode}$ and $\Delta J_{\rm mode}$ are explicitly given by

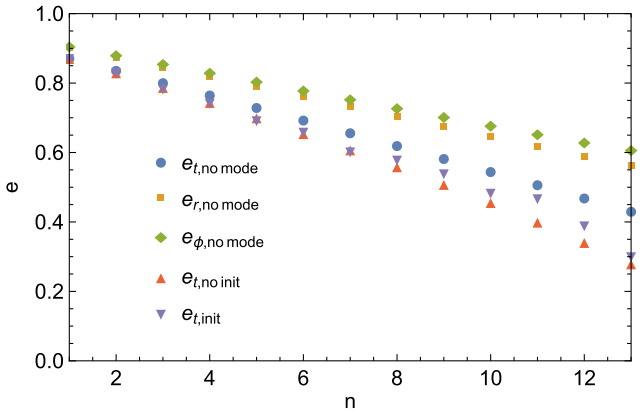

FIG. 5. Plot of PN eccentricities for a sequence of pericenter passages, indexed by n. The quantities e_t, e_r, and e_ϕ are not gauge invariant and their values are given in modified harmonic coordinates. The initial pericenter separation is $R_{0,1} = 3R_*$, and the initial e_r is set to 0.9. The quantities $e_{\rm t,no\ mode}$, $e_{\rm r,no\ mode}$, and $e_{\phi,\rm no\ mode}$ are obtained without including the star's oscillations; $e_{\rm t,no\ init}$ is computed including the star's oscillation but zero $A_{\rm init}$; $e_{\rm t,init}$ is computed taking into account the evolution of the mode amplitude over time.

$$\begin{aligned} \Delta J_{\rm mode,z} = |Q^{22}_\xi|^2\frac{3\pi}{5\omega_{22}}\frac{M_*^2}{n^2a_r^6}[P^2_{-2}(\omega_{22})-P^2_2(\omega_{22})] \\ +\frac{2\sqrt{6\pi/5}M_*}{a_r^3 n}[P_{-2}(\omega_{22})+P_2(\omega_{22})]{\rm Im}[A^{(22)}_{\rm init}Q^{22}_\xi] \\ +\frac{2\sqrt{6\pi/5}M_*}{\omega_{22}a_r^3 n}[P_{-2}(\omega_{22})-P_2(\omega_{22})]{\rm Re}[\dot{A}^{(22)}_{\rm init}Q^{22}_\xi], \end{aligned} \tag{70}$$

and

$$\begin{aligned} \Delta E_{\rm mode} = |Q^{22}_\xi|^2\frac{3\pi}{5}\frac{M_*^2}{n^2a_r^6}[P^2_{-2}(\omega_{22})+P^2_2(\omega_{22})] \\ +|Q^{20}_\xi|^2\frac{2\pi}{5}\frac{M_*^2}{n^2a_r^6}P^2_0(\omega_{20}) \\ +\frac{\omega_{22}\sqrt{6\pi/5}M_*}{a_r^3 n}[P_{-2}(\omega_{22})-P_2(\omega_{22})]{\rm Im}[A^{(22)}_{\rm init}Q^{22}_\xi] \\ +\frac{\sqrt{6\pi/5}M_*}{a_r^3 n}[P_{-2}(\omega_{22})+P_2(\omega_{22})]{\rm Re}[\dot{A}^{(22)}_{\rm init}Q^{22}_\xi] \\ -\frac{2\sqrt{\pi/5}M_*}{a_r^3 n}\dot{A}^{(20)}_{\rm init}Q^{20}_\xi P_0(\omega_{20}). \end{aligned} \tag{71}$$

Note that in order to capture higher-PN tidal effects, the analysis of stellar oscillation in the Appendix should be extended to higher-PN orders as well. In order to illustrate the trajectory model described by Eqs. (32), (33), (65), (66), (63), and (64), we start an orbit with initial pericenter distance $R_0 = 3R_*$ and initial eccentricity $e_r = 0.9$ (in modified harmonic coordinates; this quantity is not gauge invariant). In Fig. 5, we compare the evolution of eccentricities in three different scenarios: (i) assuming no tidal excitations of the stars, (ii) allowing stellar oscillations, while neglecting the nonzero values of $A_{\rm init}$ and $\dot{A}_{\rm init}$ from previous encounters, and (iii) allowing star oscillations and evolving $A_{\rm init}$ and $\dot{A}_{\rm init}$. In Fig. 6, we also present the evolution of the orbital period, pericenter frequency, and

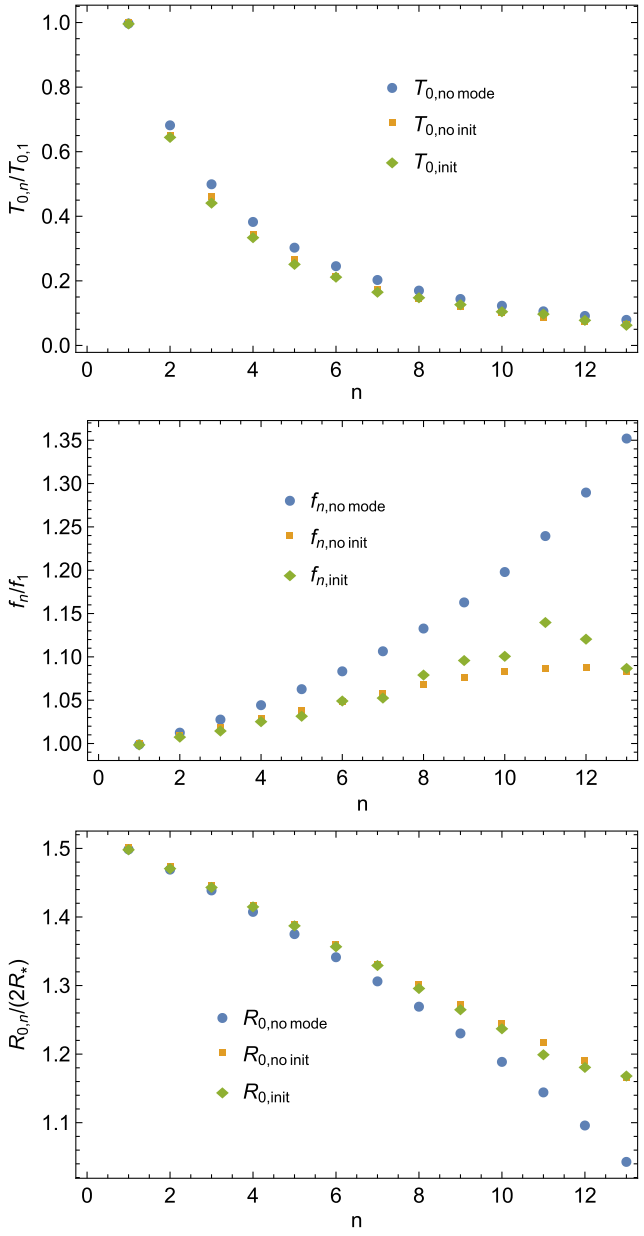

FIG. 6. The same setup as in Fig. 5. The top plot represents the evolution of the orbital period; the middle panel represents the evolution of the pericenter frequency; the bottom panel represents the evolution of the pericenter distance.

pericenter distance for the above three scenarios. We can see that for such a close encounter, the oscillation of the stars significantly alters the trajectory, and it is important to include the evolution of the modes in the trajectory model. In fact, for this case during some of the later close encounters, the frequency of the orbit is larger when this evolution is tracked, compared to when it is not, as energy and angular momentum are taken out of the NS oscillations and put back into the orbit. We also notice that, for the last several orbits, the eccentricity falls below 0.5. Strictly speaking, orbits in such a regime are no longer highly eccentric, since the impulsive approximation is no longer accurate. To deal with orbits with midrange eccentricities, the mode evolution has to be computed using a continuous forcing in time. Studying this regime is beyond the scope of this paper.

VI. CONCLUSION

In this work, we have shown that the tidal excitation of stellar modes can dramatically influence the dynamics of binary neutron stars in highly eccentric orbits. The amount of extra energy and angular momentum change in the orbit due to mode excitation can be tens of percent of that due to GWs alone, if the pericenter distance is smaller than $\sim 4R_*$. The exact amounts will depend on the EOS, and here we focused on a $\Gamma = 2$ polytrope to simplify the comparison between the analytic model and numerical results. The formalism describing the mode excitation and orbital evolution, however, applies for generic EOSs (cf. Sec. II). The prediction from the Newtonian approximation agrees with the full numerical results to within a factor of a 2 (with the error likely dominated by systematic effects in measuring orbital properties from the code results). This also resolves the large discrepancy between a similar analytic calculation and numerical simulations reported in Ref. [37].

The discussion presented in this work also applies for highly eccentric NS-BH binaries, regardless of the mass ratio [60]. While the rates of detecting these highly eccentric binaries are uncertain, their gravitational waveforms display distinctive f-mode oscillations, which are not present in any appreciable amount in quasicircular systems. Observing these oscillations would provide unprecedented information about the structure and EOS of cold NSs. One possible way to enhance the SNR of these oscillation features is to stack the post-encounter waveform of a series of pericenter passages, which requires accurate predictions for the timing of these encounters. Another possibility is to rely on the observation of third-generation ground-based detectors. As the f-mode frequency is generally above 1 kHz (the f-mode frequency in Fig. 3 is approximately 2.1 kHz), the high-frequency detector proposed in Ref. [61] is ideal for observing such signals. Assuming a detection strategy that coherently adds the signals from different pericenter encounters, the estimated SNR for f-mode oscillations is

$$\text{SNR} \sim 30\left(\frac{\mathcal{E}_{mode}}{\mathcal{E}_{\text{GW}}}\right)^{1/2}\left(\frac{50\ \text{Mpc}}{d}\right)\left(\frac{5\times 10^{-25}\ \text{Hz}^{-1/2}}{\sqrt{S_n}}\right) \times \left(\frac{2000\ \text{Hz}}{f}\right), \tag{72}$$

where d is the distance of the binary from Earth, S_n is the one-sided power spectral density of the detector, $\mathcal{E}_{\text{GW}}$ is the

total energy radiated by GWs and $\mathcal{E}_{mode}$ is the energy radiated by f-mode oscillations.

ACKNOWLEDGMENTS

The authors thank Nathan K. Johnson-McDaniel, Coleman Miller and Cecilia Chirenti for interesting discussions. F. P., V. P., and H. Y. acknowledge support from National Science Foundation (NSF) Grant No. PHY-1607449, the Simons Foundation, Natural Sciences and Engineering Research Council (NSERC) and the Canadian Institute For Advanced Research (CIFAR). V. P. also acknowledges support from National Aeronautics and Space Administration (NASA) Grant No. NNX16AR67G (Fermi). This research was supported in part by the Perimeter Institute for Theoretical Physics. Research at Perimeter Institute is supported by the Government of Canada through the Department of Innovation, Science and Economic Development Canada and by the Province of Ontario through the Ministry of Research, Innovation and Science. Computational resources were provided by XSEDE under Grant No. TG-PHY100053 and the Perseus cluster at Princeton University.

APPENDIX: PERTURBATIONS OF A POLYTROPIC STAR

The perturbation of a polytropic star is described by the Lagrangian displacement field $\boldsymbol{\xi}$, which obeys [Eq. (2.212) of Ref. [62]]

$$\partial_t^2\xi = \left(\frac{\delta\rho}{\rho^2}\right)\nabla\rho - \frac{\nabla\delta p}{\rho} - \nabla\delta\Phi, \tag{A1}$$

where

$$\begin{aligned}\delta p &= -\Gamma_p p\nabla\cdot\xi - \xi\cdot\nabla p,\\ \delta\rho &= -\nabla\cdot(\rho\xi).\end{aligned} \tag{A2}$$

Here Γ_p is the adiabatic index of the perturbation, which may or may not be the same as Γ for the equilibrium configuration. However, for the polytropic (hence barotropic) stars studied here, we have $\Gamma = \Gamma_p$. In addition, the total Newtonian potential is $\delta\Phi = \delta U + U_{\rm tide}$, where δU obeys the Poisson equation:

$$\nabla^2\delta U = -4\pi G\delta\rho. \tag{A3}$$

The equation of motion for the Lagrangian displacement field can be written schematically as

$$\partial_t^2\xi_j + L_j{}^k\xi_k = \nabla_j U_{\rm tide}. \tag{A4}$$

In order to determine the body's response to an applied tidal field, it is useful to first compute the normal modes of the system, corresponding to free oscillations, i.e., solutions of Eq. (A4) with the right-hand side being zero. With $\xi^{(n)}$ given in Eq. (5), we write ξ_j as $\xi_j^{(n)}e^{i\sigma t}$, and define

$$\begin{aligned}\delta p &= \rho(r)y(r)Y_{lm}(\theta,\phi)e^{i\sigma t},\\ \delta\rho &= \varrho(r)Y_{lm}(\theta,\phi)e^{i\sigma t},\\ \delta U &= u(r)Y_{lm}(\theta,\phi)e^{i\sigma t}.\end{aligned} \tag{A5}$$

When combining Eqs. (A1) and (A3), we notice that not all perturbation variables are independent. In particular, we can express ξ_S and ϱ in terms of the other variables as

$$\xi_S = \frac{y+u}{r\sigma^2}, \qquad \varrho = \frac{\rho^2 y}{\Gamma_p p} - A\xi_R. \tag{A6}$$

We obtain the following ordinary differential equations:

$$\begin{aligned}(r^2\xi_R)' &= -\frac{r^2 p'\xi_R}{\Gamma_p p} + \left[\frac{l(l+1)}{\sigma^2} - \rho\frac{r^2}{\Gamma_p p}\right]y + \frac{l(l+1)u}{\sigma^2},\\ y' &= (\sigma^2 + Ag)\xi_R - Ay - u',\\ u'' &= -\frac{2}{r}u' + \frac{l(l+1)u}{r^2} + 4\pi G\rho\left(\frac{\rho y}{\Gamma_p p} - A\xi_R\right)\end{aligned} \tag{A7}$$

with

$$g \equiv -\frac{p'}{p}, \qquad A \equiv \frac{\rho'}{\rho} - \frac{p'}{\Gamma_p p}. \tag{A8}$$

As explained above, for the polytropic stars studied here, A is zero. The differential equations are subject to the regularity condition at the center of the star and boundary conditions at the stellar surface which require force balance and zero pressure:

$$\begin{aligned}(\rho y + p'\xi_R)|_{R_*} &= 0,\\ \left(u' + (l+1)\frac{u}{r}\right)\Big|_{R_*} &= -4\pi G\rho(R_*)\xi_R(R_*).\end{aligned} \tag{A9}$$

The eigenfrequency σ and eigenfunctions ξ_R and ξ_S can be obtained by solving Eq. (A7) with the above boundary conditions.

[1] B. P. Abbott *et al.* (Virgo and LIGO Scientific Collaborations), Phys. Rev. Lett. **116**, 061102 (2016).
[2] B. P. Abbott *et al.* (Virgo and LIGO Scientific Collaborations), Phys. Rev. Lett. **116**, 241103 (2016).
[3] B. P. Abbott *et al.* (Virgo and LIGO Scientific Collaborations), Phys. Rev. Lett. **118**, 221101 (2017).
[4] B. Abbott *et al.*, Astrophys. J. Lett. **851**, L35 (2017).
[5] B. P. Abbott *et al.*, Phys. Rev. Lett. **119**, 141101 (2017).
[6] B. P. Abbott *et al.*, Phys. Rev. Lett. **119**, 161101 (2017).
[7] R. M. O'Leary, B. Kocsis, and A. Loeb, Mon. Not. R. Astron. Soc. **395**, 2127 (2009).
[8] W. H. Lee, E. Ramirez-Ruiz, and G. van de Ven, Astrophys. J. **720**, 953 (2010).
[9] B. Kocsis and J. Levin, Phys. Rev. D **85**, 123005 (2012).
[10] A. Fabian, J. Pringle, and M. Rees, Mon. Not. R. Astron. Soc. **172**, 15P (1975).
[11] D. Pooley *et al.*, Astrophys. J. Lett. **591**, L131 (2003).
[12] J. Samsing, M. MacLeod, and E. Ramirez-Ruiz, Astrophys. J. **784**, 71 (2014).
[13] C. L. Rodriguez, M. Morscher, B. Pattabiraman, S. Chatterjee, C.-J. Haster, and F. A. Rasio, Phys. Rev. Lett. **115**, 051101 (2015).
[14] J. Samsing, Phys. Rev. D **97**, 103014 (2018).
[15] W. E. East, S. T. McWilliams, J. Levin, and F. Pretorius, Phys. Rev. D **87**, 043004 (2013).
[16] L. Wen, Astrophys. J. **598**, 419 (2003).
[17] N. Seto, Phys. Rev. Lett. **111**, 061106 (2013).
[18] S. Naoz, Annu. Rev. Astron. Astrophys. **54**, 441 (2016).
[19] F. Antonini, S. Toonen, and A. S. Hamers, Astrophys. J. **841**, 77 (2017).
[20] C. L. Rodriguez and F. Antonini, arXiv:1805.08212.
[21] M. Turner, Astrophys. J. **216**, 914 (1977).
[22] R. Gold, S. Bernuzzi, M. Thierfelder, B. Brügmann, and F. Pretorius, Phys. Rev. D **86**, 121501 (2012).
[23] W. E. East, F. Pretorius, and B. C. Stephens, Phys. Rev. D **85**, 124009 (2012).
[24] W. E. East and F. Pretorius, Astrophys. J. **760**, L4 (2012).
[25] D. Tsang, Astrophys. J. **777**, 103 (2013).
[26] V. Paschalidis and N. Stergioulas, Living Rev. Relativity **20**, 7 (2017).
[27] L. Baiotti and L. Rezzolla, Rep. Prog. Phys. **80**, 096901 (2017).
[28] C. Barat, R. Hayles, K. Hurley, M. Niel, G. Vedrenne, U. Desai, V. Kurt, V. Zenchenko, and I. Estulin, Astron. Astrophys. **126**, 400 (1983).
[29] R. C. Duncan, Astrophys. J. Lett. **498**, L45 (1998).
[30] C. Thompson, H. Yang, and N. Ortiz, Astrophys. J. **841**, 54 (2017).
[31] H. Yang, K. Yagi, J. Blackman, L. Lehner, V. Paschalidis, F. Pretorius, and N. Yunes, Phys. Rev. Lett. **118**, 161101 (2017).
[32] H. Yang, V. Paschalidis, K. Yagi, L. Lehner, F. Pretorius, and N. Yunes, Phys. Rev. D **97**, 024049 (2018).
[33] E. Berti, K. Yagi, H. Yang, and N. Yunes, Gen. Relativ. Gravit. **50**, 49 (2018).
[34] S. Bose, K. Chakravarti, L. Rezzolla, B. S. Sathyaprakash, and K. Takami, Phys. Rev. Lett. **120**, 031102 (2018).
[35] R. Brito, A. Buonanno, and V. Raymond, arXiv:1805.00293.
[36] A. Parisi and R. Sturani, Phys. Rev. D **97**, 043015 (2018).
[37] C. Chirenti, R. Gold, and M. C. Miller, Astrophys. J. **837**, 67 (2017).
[38] N. Loutrel and N. Yunes, Classical Quantum Gravity **34**, 135011 (2017).
[39] E. A. Huerta *et al.*, Phys. Rev. D **95**, 024038 (2017).
[40] S. E. Gralla, Classical Quantum Gravity **35**, 085002 (2018).
[41] L. Blanchet, Living Rev. Relativity **17**, 2 (2014).
[42] W. Press and S. Teukolsky, Astrophys. J. **213**, 183 (1977).
[43] E. Poisson and I. Vlasov, Phys. Rev. D **81**, 024029 (2010).
[44] H. Yang and M. Casals, Phys. Rev. D **96**, 083015 (2017).
[45] P. C. Peters, Phys. Rev. **136**, B1224 (1964).
[46] V. Paschalidis, W. E. East, F. Pretorius, and S. L. Shapiro, Phys. Rev. D **92**, 121502 (2015).
[47] W. E. East, V. Paschalidis, F. Pretorius, and S. L. Shapiro, Phys. Rev. D **93**, 024011 (2016).
[48] W. E. East, V. Paschalidis, and F. Pretorius, Classical Quantum Gravity **33**, 244004 (2016).
[49] W. E. East, F. Pretorius, and B. C. Stephens, Phys. Rev. D **85**, 124010 (2012).
[50] W. E. East, F. M. Ramazanoglu, and F. Pretorius, Phys. Rev. D **86**, 104053 (2012).
[51] S. V. Chaurasia, T. Dietrich, N. K. Johnson-McDaniel, M. Ujevic, W. Tichy, and B. Brgmann, arXiv:1807.06857.
[52] M. G. Alford, L. Bovard, M. Hanauske, L. Rezzolla, and K. Schwenzer, Phys. Rev. Lett. **120**, 041101 (2018).
[53] M. G. Alford, S. Mahmoodifar, and K. Schwenzer, J. Phys. G **37**, 125202 (2010).
[54] E. Huerta, P. Kumar, S. T. McWilliams, R. O'Shaughnessy, and N. Yunes, Phys. Rev. D **90**, 084016 (2014).
[55] T. Damour and G. Schäeer, Nuovo Cimento Soc. Ital. Fis. **101B**, 127 (1988).
[56] G. Schäfer and N. Wex, Phys. Lett. A **174**, 196 (1993).
[57] N. Wex, Classical Quantum Gravity **12**, 983 (1995).
[58] R.-M. Memmesheimer, A. Gopakumar, and G. Schäfer, Phys. Rev. D **70**, 104011 (2004).
[59] K. Arun, L. Blanchet, B. R. Iyer, and S. Sinha, Phys. Rev. D **80**, 124018 (2009).
[60] H. Yang, W. E. East, and L. Lehner, Astrophys. J. **856**, 110 (2018).
[61] H. Miao, H. Yang, and D. Martynov, arXiv:1712.07345.
[62] E. Poisson and C. M. Will, *Gravity* (Cambridge University Press, Cambridge, England, 2014).